Long-Term Continuously Updated Deformation Time Series From Multisensor InSAR in Xi'an, China From 2007 to 2021

Baohang Wang, *Student Member, IEEE*, Chaoying Zhao, *Senior Member, IEEE*, Qin Zhang, *Member, IEEE*,
Zhong Lu, *Senior Member, IEEE*, and Antonio Pepe, *Senior Member, IEEE*

***Abstract*—According to historical records, land subsidence has been occurring in Xi'an, China, since the 1960s, characterized by complex land subsidence patterns. This subsidence has the potential to cause serious societal and economic problems during the process of urbanization. Long-term, large-scale monitoring and dynamic high precision tracking of the evolution of surface deformation associated with geohazards is a prerequisite for effective prevention or advance warning of geological disasters. Synthetic aperture radar interferometry (InSAR), a satellite remote sensing technology, can facilitate such monitoring. Both currently operating and planned SAR satellites would provide extensive amounts of SAR data. In this article, we describe an approach for continuously updating long-term multisensor InSAR deformation time series using robust sequential least squares. It is successfully applied to near-real-time monitoring of the long-term evolution of surface deformation in Xi'an, China, from January 3, 2007 to February 12, 2021, using four SAR satellites: ALOS/PALSAR-1, TerraSAR-X, ALOS/PALSAR-2, and Sentinel-1A. In order to analyze deformation evolution, temporal independent component analysis was used to interpret deformation patterns. We found that land subsidence in Xi'an has slowed and even halted in some areas. However, large areas are uplifting, which presents a potential for geohazards. We conclude that the proposed approach using continuously updated deformation time series from multisensor InSAR can provide near-real-time deformation measurements, which are necessary for an early warning system.**

***Index Terms*—Independent component analysis (ICA), multisensor synthetic aperture radar interferometry (InSAR), robust sequential least squares (RSLS), surface deformation update.**

I. INTRODUCTION

INTERFEROMETRIC synthetic aperture radar (InSAR) is playing an increasingly critical role in investigating the deformation of the Earth's surface. Over the last 30 years, InSAR has been used to reconstruct historical surface deformation [1] and has been successfully used to monitor the surface deformation caused by various geohazards such as earthquakes [2], volcanoes [3], landslides [4], and land subsidence [5].

During urbanization, land subsidence in urban areas can seriously damage surrounding buildings, reducing safety, and causing significant societal and economic harm. InSAR technology can investigate surface deformation over large scales and with high precision. It has been used to investigate surface deformation in Las Vegas [6] and Houston–Galveston, USA [7], Mexico City, Mexico [8], northeast Iran [9], the West Thessaly Basin, Greece [10], the Pisa Urban area, Italy [11], and Beijing [12], amongst others. Overexploitation of groundwater is a principal cause of land subsidence.

Over the last few decades, several multitemporal InSAR algorithms have been developed [13]–[23], which can be divided into two main families. The first group is based on the single-master permanent scatterer (PS) InSAR technique [13], which uses highly reflective objects (e.g., human-made infrastructure in urban areas) that preserve high coherence and phase stability even in large temporal and perpendicular baseline synthetic aperture radar (SAR) data pairs. The second group comprises multiple-master small baseline subset (SBAS) InSAR techniques [14] that use distributed scatterers (DSs), which are distributed over resolution cells at multiple resolutions and are characterized by varying coherence and phase stability. Expanded PS and SBAS algorithms have been developed for deformation time-series analysis and are described in detail in [24] and [25]. Correct identification of DSs and phase optimization is required, for which several techniques have been proposed [26]. When applying InSAR technology to long-term continuous land subsidence investigation and time-series analysis, the SBAS technique can mitigate the effects of decorrelation by the short-temporal-space baseline interferogram pair, especially in regions suffering from heavy decorrelation, a large deformation gradient, and a long time horizon. Thus, it is well suited to investigate long-term surface deformation. The onboard SAR satellites (Sentinel-1A/B, ALOS/PALSAR-2, TerraSAR-X/TanDEM-X,

Manuscript received May 3, 2021; revised June 19, 2021 and July 2, 2021; accepted July 10, 2021. Date of publication July 14, 2021; date of current version July 30, 2021. This work was supported in part by the National Natural Science Foundation of China under Grant 41874005, Grant 41731066, and Grant 41929001 and in part by the Fundamental Research Funds for the Central Universities under Grant 300102269303 and Grant 300102269719. *(Corresponding authors: Chaoying Zhao; Qin Zhang.)*

Baohang Wang, Chaoying Zhao, and Qin Zhang are with the School of Geological Engineering and Geomatics, Chang'an University, Xi'an 710054, China (e-mail: wangbaohang@chd.edu.cn; zhaochaoying@163.com; dczhangq@chd.edu.cn).

Zhong Lu is with the M. Huffington Department of Earth Sciences, Southern Methodist University, Dallas, TX 75275 USA (e-mail: zhonglu@mail.smu.edu).

Antonio Pepe is with the National Research Council of Italy, Institute for the Electromagnetic Sensing of the Environment (CNR-IREA), 80124 Napoli, Italy (e-mail: pepe.a@irea.cnr.it).

Digital Object Identifier 10.1109/JSTARS.2021.3096996

COSMO-SkyMed, and Radarsat-2), in combination with planned SAR satellites, will provide a significant quantity of data and shortened intervals between revisits. Using multiple sensors to investigate surface deformation affords two outcomes. The first is a 2-D or 3-D surface deformation rate and a resulting deformation time series. The second is the ability to fuse the deformation rate or the deformation time series with higher temporal resolution. In previous studies, combined multisensor SAR data have been used to monitor land subsidence [27], volcano deformation [28], and landslides [29]. Other applications of multisensor, multitrack, and multidimensional deformation are summarized in [30] and [31].

The fusion of multisensor SAR data to rapidly estimate deformation time series can improve the frequency of deformation time-series production, which facilitates obtaining early warning of disasters. To this end, parallel computation and cloud computing were used to accelerate the processing of InSAR data [32]. The Kalman filter has been used to update deformation time series [33], [34]; however, inaccurate deformation prediction information can easily lead to deviations in deformation time series. The sequential filtering method was developed to optimize the DS phase and avoid computational burden using full interferograms [35]. Sequential SAR data registration [36], [37] has been proposed for Sentinel-1 TOPSAR images. Sequential least squares (SLS) and complex SLS methods have been used to dynamically update deformation parameters for single SAR sensors, including line-of-sight (LOS) deformation time series [38] and 2-D offset tracking deformation time series [39], without the loss of accuracy as compared with conventional SBAS-InSAR and PO-SBAS (Pixel offset SBAS), respectively.

In this era of massive and diverse SAR data availability, how can we process multisensor SAR data simultaneously and provide deformation time series as quickly and precisely as possible? We propose a robust sequential least squares (RSLS) algorithm, which processes multisensor SAR data simultaneously to dynamically update and improve the temporal resolution of deformation time series. Fusing multisensor SAR data can assist in providing early warning of disasters.

In this study, using vertical deformation as seen in land subsidence/uplift as an example, we devised an approach to continuously update multisensor InSAR deformation time series in order to monitor in near-real-time the long-term evolution of surface deformation in Xi'an, China. We applied the approach over a 13-year study period from January 3, 2007 to February 12, 2021, using four SAR satellites. In order to analyze deformation evolution, temporal independent component analysis (ICA) was used to interpret deformation patterns. We focus on time-series analysis and found that the land subsidence rate in Xi'an is slowing, with a future trend of uplift deformation.

II. STUDY AREA AND DATA

A. Study Area

Xi'an is located to the north of the Qinling Mountains, in the vicinity of the Loess Plateau in China. It is bounded by the Chan River and Ba River to the east, the Feng River to the west, and the Wei River to the north. Loess ridges and depressions are interchangeably distributed in central urban areas (see Fig. 1).

Since the 1960s, Xi'an has suffered from severe land subsidence and ground fissure hazards [41]. Economic development and urbanization have led to more than 50 years of excessive groundwater exploitation [41]. Subsequently, 14 ground fissures formed, accompanied by land subsidence [42]. The Chang'an-Lintong fault (CAF), which runs mainly in the ENE direction, controls the activities of the 14 ground fissures. The interaction between these fissures and land subsidence areas has developed into elliptical-shaped surface subsidence [43].

Large-scale InSAR data have been used to investigate the spatiotemporal characteristics of subsidence and ground fissures in Xi'an. These include global positioning system and InSAR observations from 2005 to 2006 [44]: Envisat, ALOS, and TerraSAR SAR datasets from 2005 to 2012 [45]; ERS, Envisat, and Sentinel SAR datasets from 2003 to 2017 [46]; ALOS, TerraSAR, and Sentinel SAR datasets from 2012 to 2018 [47]; and Sentinel SAR datasets from 2015 to 2019 [40]. These studies showed that degradation of the aquifer system had led to complex subsidence and ground fissures.

B. Satellite SAR Data

Our study used 192 SAR images, including 22 from ALOS/PALSAR-1 with 4.6 × 3.1 m in range and azimuth (from January 30, 2007 to February 10, 2011), 46 from TerraSAR-X with 0.9 × 1.8 m (from October 5, 2011 to 28 May 2015), 9 from ALOS/PALSAR -2 with 4.2 × 3.2 m (from September 6, 2014 to October 28, 2017), and 115 from Sentinel-1A with 2.3 × 13.9 m (from June 20, 2015 to February 12, 2021) (see Fig. 2).

III. METHODOLOGY

A. Updating Multisensor InSAR Deformation Time Series

Phase unwrapping of interferogram is a key step in InSAR data processing [18], [21], [48], [49]. Yu *et al.* [50] reviewed the progress of InSAR phase unwrapping. After correcting digital elevation model (DEM) error, atmospheric artifacts, and orbital error for unwrapped interferograms, we used the L1-norm approach to alleviate the gross error caused by phase unwrapping, using $\boldsymbol{V}_1 = \mathbf{A}_1\boldsymbol{X} - \boldsymbol{L}_1, \mathbf{P}_1$, in which $\boldsymbol{V}_1$ is the measurement noise; $\mathbf{A}_1$ is the design matrix with -1, 0, and 1; $\boldsymbol{L}_1$ is the measurement data (unwrapped interferograms); and $\mathbf{P}_1$ is the weight matrix. This can be solved using the iteratively reweighted least squares (IRLS) method with the equivalent weight matrix $\bar{\mathbf{P}}_1$ [51]. The deformation time series is initialized using $\boldsymbol{X}^{(1)} = (\mathbf{A}_1{}^T\overline{\mathbf{P}}_1\mathbf{A}_1)^{-1}\mathbf{A}_1{}^T\overline{\mathbf{P}}_1\boldsymbol{L}_1$ and $\overline{\boldsymbol{Q}}_{X^{(1)}} = (\mathbf{A}_1{}^T\overline{\mathbf{P}}_1\mathbf{A}_1)^{-1}$ as the parameter $\boldsymbol{X}$ and its cofactor matrix for archived data, respectively.

Once we obtain a new SAR image, we first form interferograms by combining the new SAR image with recent past acquisitions. Using the SBAS strategy, we extract common pixels (as archived data) to produce phase unwrapping and error correction. Then, we have a new observation $\boldsymbol{L}_2$ (unwrapped interferograms). To estimate parameters $\boldsymbol{X}$ and $\boldsymbol{Y}$, we model the new observation with the design matrices $\mathbf{A}_2$ and $\boldsymbol{B}$, and weight

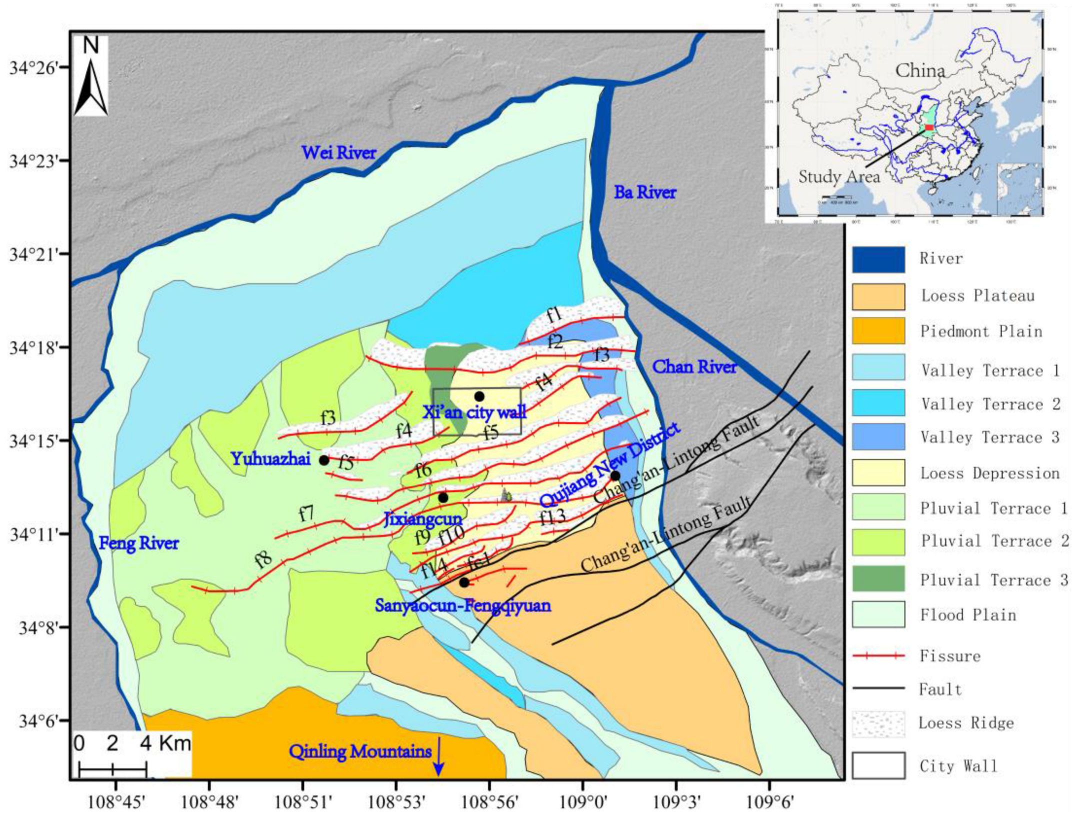

Fig. 1. Quaternary geology map of Xi’an [40].

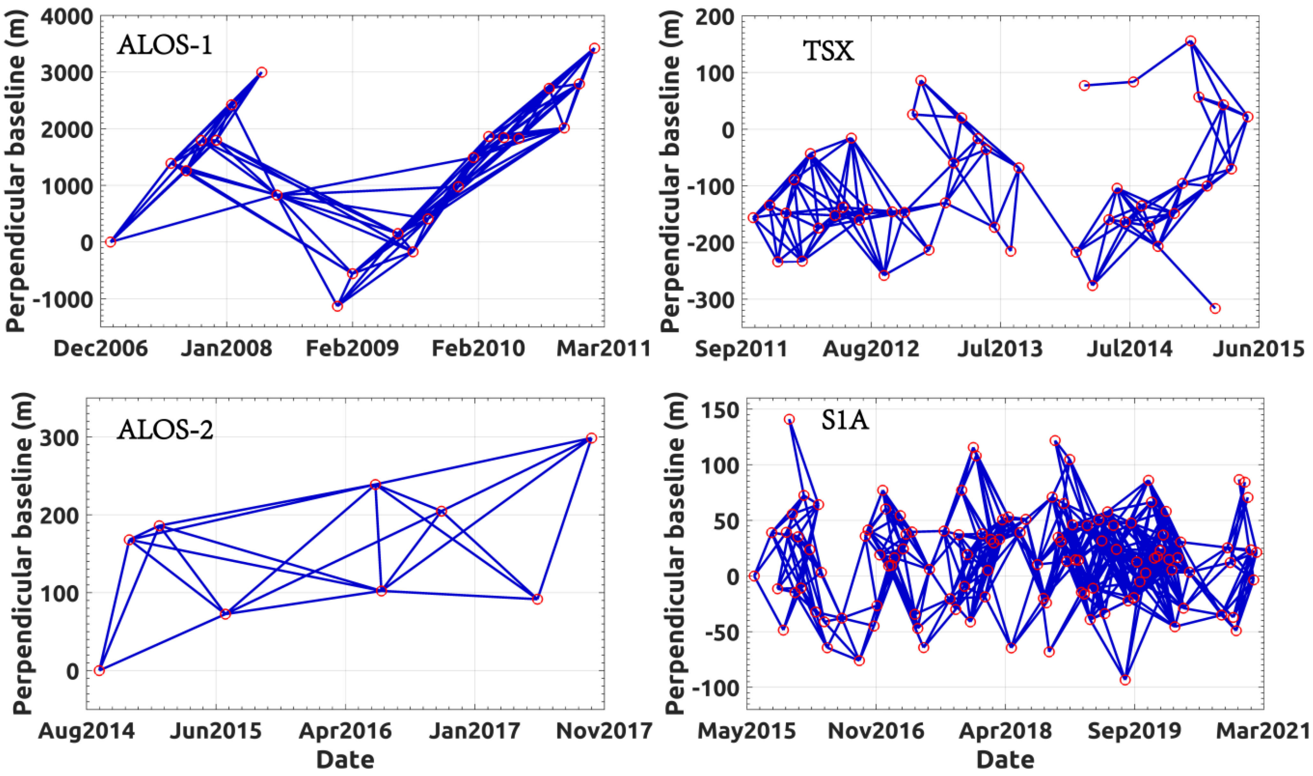

Fig. 2. Temporal and perpendicular baseline map of data from four SAR sensors used in this study.

matrix $\mathbf{P}_2$ as

$$\boldsymbol{V}_2 = \begin{bmatrix} \mathbf{A}_2 & \boldsymbol{B} \end{bmatrix} \begin{bmatrix} \boldsymbol{X}^{(2)} \\ \boldsymbol{Y} \end{bmatrix} - \boldsymbol{L}_2 \,,\ \mathbf{P}_2 \tag{1}$$

where $\boldsymbol{X}^{(2)}$ and $\boldsymbol{Y}$ are the new estimation of parameter $\boldsymbol{X}$ and cumulative deformation, respectively, at the new SAR acquisition date.

Similarly, for the L1-norm approach, arg min $\|\mathbf{V}_2\|_1$ is used to determine the weight matrix $\overline{\mathbf{P}}_2$ in order to alleviate the gross error in (1). The number of newly unwrapped interferograms in (1) is usually small, which is likely to lead to an ill-conditioned problem. According to the principle of least squares Bayesian estimation theory [52], it holds that

$$\boldsymbol{V}_2^T \overline{\mathbf{P}}_2 \boldsymbol{V}_2 + (\boldsymbol{X}^{(2)} - \boldsymbol{X}^{(1)})^T \overline{\boldsymbol{Q}}_{X^{(1)}}^{-1} (\boldsymbol{X}^{(2)} - \boldsymbol{X}^{(1)}) = \min . \tag{2}$$

Therefore, we can take $\boldsymbol{X}^{(1)}$ and $\overline{\boldsymbol{Q}}_{X^{(1)}}$ as *a priori* information of the estimated parameter $\boldsymbol{X}^{(2)}$ to calculate the equivalent weight matrix $\overline{\mathbf{P}}_2$ and update the deformation time series $[\boldsymbol{X}^{(2)}\boldsymbol{Y}]^{\mathrm{T}}$ and its cofactor matrix $\overline{\boldsymbol{Q}}_{[X^{(2)};Y]}$ as follows [38]:

$$\begin{bmatrix} \boldsymbol{X}^{(2)} \\ \boldsymbol{Y} \end{bmatrix} = \begin{bmatrix} \bar{\boldsymbol{Q}}_{X^{(1)}}^{-1} + \mathbf{A}_2{}^T \bar{\mathbf{P}}_2 \mathbf{A}_2 & \mathbf{A}_2{}^T \bar{\mathbf{P}}_2 \mathbf{B} \\ \mathbf{B}^T \bar{\mathbf{P}}_2 \mathbf{A}_2 & \mathbf{B}^T \bar{\mathbf{P}}_2 \mathbf{B} \end{bmatrix}^{-1} \times \begin{bmatrix} \bar{\boldsymbol{Q}}_{X^{(1)}}^{-1} \boldsymbol{X}^{(1)} + \mathbf{A}_2^T \bar{\mathbf{P}}_2 \boldsymbol{L}_2 \\ \mathbf{B}^T \bar{\mathbf{P}}_2 \boldsymbol{L}_2 \end{bmatrix}$$

$$\bar{\boldsymbol{Q}}_{[X^{(2)};Y]} = \begin{bmatrix} \bar{\boldsymbol{Q}}_{X^{(1)}}^{-1} + \mathbf{A}_2{}^T \bar{\mathbf{P}}_2 \mathbf{A}_2 & \mathbf{A}_2{}^T \bar{\mathbf{P}}_2 \mathbf{A}_2 \\ \mathbf{B}^T \bar{\mathbf{P}}_2 \mathbf{A}_2 & \mathbf{B}^T \bar{\mathbf{P}}_2 \mathbf{B} \end{bmatrix}^{-1} . \tag{3}$$

To avoid obtaining a large-scale inverse matrix, we use matrix inversion theory [38], [53] to solve (3)

$$\begin{aligned}
\begin{bmatrix} \boldsymbol{X}^{(2)} \\ \boldsymbol{Y} \end{bmatrix} &= \begin{bmatrix} \boldsymbol{X}^{(1)} + \mathbf{J}_x (\bar{\boldsymbol{L}}_2 - \mathbf{B}\boldsymbol{Y}) \\ (\mathbf{B}^T \bar{\boldsymbol{Q}}_J{}^{-1} \mathbf{B})^{-1} \mathbf{B}^T \bar{\boldsymbol{Q}}_J{}^{-1} (\boldsymbol{L}_2 - \mathbf{A}_2 \boldsymbol{X}_1) \end{bmatrix} \\
\bar{\boldsymbol{Q}}_{[X^{(2)};Y]} &= \begin{bmatrix} \bar{\boldsymbol{Q}}_{X^{(2)}} & \bar{\boldsymbol{Q}}_{\mathrm{X}^{(2)},\mathrm{Y}} \\ \bar{\boldsymbol{Q}}^T{}_{\mathrm{X}^{(2)},\mathrm{Y}} & \bar{\boldsymbol{Q}}_Y \end{bmatrix} \\
\bar{\boldsymbol{Q}}_{X^{(2)}} &= \bar{\boldsymbol{Q}}_{X^{(1)}} - \mathbf{J}_x \mathbf{A}_2 \bar{\boldsymbol{Q}}_{X^{(1)}} + \mathbf{J}_x \mathbf{B} \bar{\boldsymbol{Q}}_Y \mathbf{B}^T \mathbf{J}_x^T \\
\bar{\boldsymbol{Q}}_{\mathrm{X}^{(2)},\mathrm{Y}} &= -\mathbf{J}_x \mathbf{B} \boldsymbol{Q}_{Y,Y} \\
\bar{\boldsymbol{Q}}_Y &= (\mathbf{B}^T \bar{\boldsymbol{Q}}_J{}^{-1} \mathbf{B})^{-1} \\
\mathbf{J}_x &= \bar{\boldsymbol{Q}}_{X^{(1)}} \mathbf{A}_2{}^T \bar{\boldsymbol{Q}}_J{}^{-1} \\
\bar{\boldsymbol{Q}}_J &= \bar{\mathbf{P}}_2^{-1} + \mathbf{A}_2 \bar{\boldsymbol{Q}}_{X^{(1)}} \mathbf{A}_2{}^T
\end{aligned} \tag{4}$$

where $[X^{(2)};Y]$ is the updated deformation time series and $\bar{\boldsymbol{Q}}_{[X^{(2)};Y]}$ is their cofactor matrix.

This technique for updating deformation time series is executed for data from additional sensors in turn. Assuming purely vertical deformation, such as when monitoring for land subsidence, there will be overlapping time periods of data measured from multiple sensors. After determining the multisensor deformation time series, we can project various deformations in the LOS direction to the vertical direction $\boldsymbol{D}_{\mathrm{Def}}^i = \frac{\boldsymbol{X}_{\mathrm{Los}}^i}{\cos(\varphi^i)}$, in which i represents different SAR sensors, $\boldsymbol{D}_{\mathrm{Def}}$ is the vertical deformation time series, and φ is incidence angle. $\boldsymbol{X}_{\mathrm{Los}}$ is the deformation time series in the LOS direction. Next, we project multisensor deformation time series into the geographic coordinate system and resample the different resolution deformation time series into the same one. We extract the common monitoring points of all sensors, pixel by pixel, to fuse the deformation time series. Specifically, we generate the deformation time series by adjusting the systematic deviation between two different sensors in the overlapping periods. We model the deviation as follows:

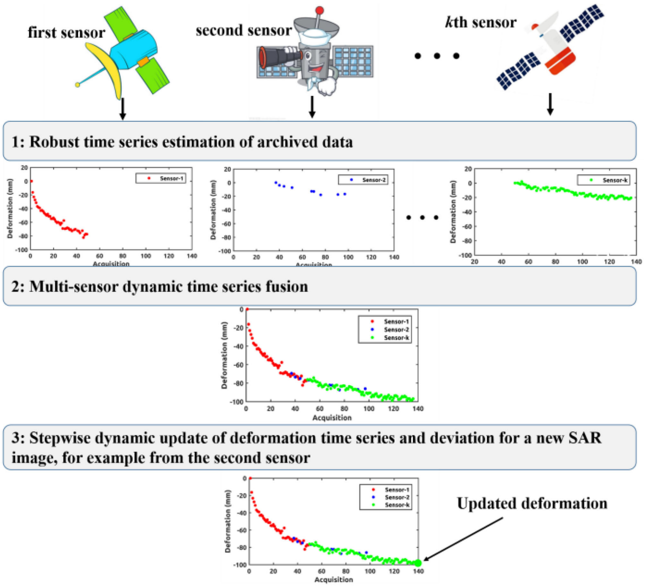

Fig. 3. Flowchart showing continuous updating of multisensor InSAR deformation time series.

$$\begin{aligned}
(\boldsymbol{X}_1 - \mathrm{d}) - \boldsymbol{X}_2 &= \boldsymbol{V} \\
\boldsymbol{V}^T \mathbf{P} \boldsymbol{V} &= \min \\
\Delta \boldsymbol{X} &= \boldsymbol{M}\mathrm{d} + \boldsymbol{V}, \mathbf{P} \\
d &= (\boldsymbol{M}^T \mathbf{P} \boldsymbol{M})^{-1} \boldsymbol{M}^T \mathbf{P} \Delta \boldsymbol{X} \\
&= \frac{1}{n} \sum_{i=1}^{n} (\boldsymbol{X}_{1,i} - \boldsymbol{X}_{2,i})
\end{aligned} \tag{5}$$

where $\boldsymbol{X}_1$ and $\boldsymbol{X}_2$ are the overlapping deformation time series from multisensor SAR data, $\boldsymbol{V}$ is the residual deformation, d is the systematic deviation between two deformation time series, and $\boldsymbol{M}$ is the design matrix. We used the least-squares criterion to fuse deformation time series within the overlapping periods, which is similar to using quantile adjustment with a cumulative distribution function [54] and overlapping data [55], to correct system deviations. Fig. 3 shows the flowchart of the automatic multisensor InSAR deformation time series.

In cases with no horizontal deformation, we use the correct datum of overlapping data among each sensor/track to fuse 1-D vertical deformation time series. Otherwise, we use multisensor, multitrack deformation time series to update multidimension deformation time series as follows:

$$\begin{bmatrix}\cos\theta_1 & -\sin\theta_1\cos\alpha_1\\ \cos\theta_2 & -\sin\theta_2\cos\alpha_2\end{bmatrix}\begin{bmatrix}D_V t_n\\ D_E t_n\end{bmatrix}=\begin{bmatrix}Dt_{n1}\\ Dt_{n2}\end{bmatrix} \tag{6}$$

where D_V and D_E are vertical and east-west deformation, θ_1 and α_1 are incident angle and heading angle, respectively, of the first sensor or track data, and θ_2 and α_2 are incident angle and heading angle, respectively, of the second sensor or track data. *t* represents the *n*th observation. t_{n1} and t_{n2} indicate the first and second sensor or track LOS cumulative deformation. It is straightforward to extend the 3-D deformation time series through the inclusion of additional observation data [30], [31].

B. Temporal ICA (tICA) Based Spatiotemporal Deformation Pattern Decomposition

Once we have obtained the long-term deformation time series over a larger area, we must determine how to identify different complex deformation characteristics. The different characteristics of InSAR-driven ground deformation time series have been studied using ICA. This method was introduced in [56] and relied on the assumption that the observed ground deformation signal can be factorized as a linear combination of statistically independent components (ICs). ICA has been used to separate atmospheric noise from signals [57] and to better understand elastic deformation [58], DEM error [59], and volcanic deformation [60]. The unique solution is derived by maximizing the mutual independence of estimating each statistically IC.

tICA assumes that terrain deformation signal sources are temporally statistically independent. In order to separate different spatiotemporal deformation patterns over large scales, tICA maximizes the statistical independence of an arbitrary number of ICs and fits different temporal patterns and spatial functions [57].

To apply tICA, we first reorganized the obtained ground deformation time series related to the set of *np* pixels well-processed coherent SAR pixels as $\mathbf{U}=[\Phi_1^{\mathrm{def}},\Phi_2^{\mathrm{def}},\ldots,\Phi_{np}^{\mathrm{def}}]^T$ with $\Phi^{\mathrm{def}}=[\phi_0^{\mathrm{def}},\phi_1^{\mathrm{def}},\ldots,\phi_{N-1}^{\mathrm{def}}]$. Each row of $\mathbf{U}$ represents the relevant ground deformation time series values and each column represents the selected coherent SAR pixels. We used the FastICA algorithm [61], [62] with a temporal model to decompose the mixed-signal matrix $\mathbf{U}$ into a set of *ns* statistically independent sources in the temporal $\mathbf{S}=[s_1,s_2,\ldots,s_{ns}]^T$ ($s_i=[s_i^0,s_i^1,\ldots,s_i^{N-1}]$) and mixing $\mathbf{A}=[a_1,a_2,\ldots,a_{ns}]$ ($a_i=[a_i^1,a_i^2,\ldots,a_i^{np}]^T$) matrices, in which $\mathbf{S}$ and $\mathbf{A}$ are unknown. In the FastICA algorithm, fixed-point iteration is employed to derive the converged solution of the mixing matrix $\mathbf{A}$ and source matrix $\mathbf{S}$ by maximizing the spatial non-Gaussianity of sources [59]. The mixing matrix $\mathbf{A}$ captures the relative contribution of each independent temporal component. Accordingly, we modeled the ground deformation time series as

$$\mathbf{U}=\mathbf{A}\mathbf{S}. \tag{7}$$

In particular, it can be shown that the relationship between a set of deformation time series $\mathbf{U}$ and the independent sources $\mathbf{S}$ of a whole study area can be expressed as

$$\mathbf{U}=\sum_{i}^{ns} a_i\times s_i \tag{8}$$

where s_i is the spatial distribution of the *i*th independent source, and a_i is the vector of the relative contribution of the corresponding source s_i. Therefore, we can use (8) for each spatial source and deformation time series.

IV. RESULTS AND ANALYSIS

A. Updating Multisensor Deformation Time Series

In this study, the terrain-related atmospheric phase was removed from the best-fitting linear relation between the phase delay and topography [63], [64]. The Generic Atmospheric Correction online service for InSAR [65] is a practical method for removing the atmospheric phase. DEM error-caused phase was estimated using the relationship between perpendicular baseline and phase $\frac{4\pi}{\lambda\sin\theta}\frac{B^{\perp}}{R}\Delta H=\mathrm{unw}$ [66], where ΔH, and unw are DEM error and unwrapped interferometric phases, respectively.λ, R, and θ are the radar wavelength, sensor-to-target distance, and incidence angle, respectively. $B^{\perp}$ is the perpendicular baseline. After the correction of DEM error, atmospheric artifacts, and orbital error in the unwrapped interferograms, we used IRLS to produce deformation time series for each set of archived sensor data. At this stage, we stored deformation time series and their cofactor matrices for postprocessing. In the case of vertical deformation, we projected LOS direction deformations from different sensors to the vertical direction and geocoded them in the same geographical coordinate system. Finally, we fused the multisensor deformation time series using overlapping data to generate long-term and high temporal resolution deformation time series.

When new SAR data become available, we are able to generate new interferograms utilizing the new SAR image and the most recently archived SAR images originating from the same sensor by setting short temporal and spatial baseline thresholds. Subsequently, we update the deformation time series for each newly acquired SAR image using (4). Fig. 4 shows the cumulative vertical deformation map obtained by fusing SAR data acquired from four different sensors between January 3, 2007 and February 12, 2021 and continuously updating the multisensor InSAR deformation time series. The data include 22 ALOS/PALSAR-1 images, 46 TerraSAR-X images, 9 ALOS/PALSAR-2 images, and 115 Sentinel-1A SAR images. The maximum land subsidence is more than 1.3 m, and several areas of subsidence can clearly be seen between two ground fissures. The reference point is the black pentagram indicated in Fig. 4.

We introduce a method to continuously update multisensor InSAR deformation time series. It can dynamically process SAR datasets from single sensors and link different deformation time series from multiple sensors simultaneously. In addition, gross errors are effectively resolved using RSLS. Therefore, the proposed method is an extension of SLS estimation.

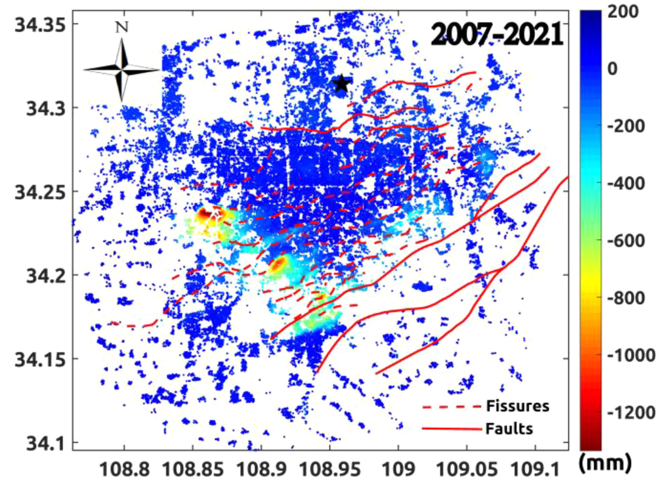

Fig. 4. Cumulative deformation from January 3, 2007 to February 12, 2021 obtained from continuously updated multisensor InSAR deformation time series from four SAR sensors. Black pentagram is a reference point.

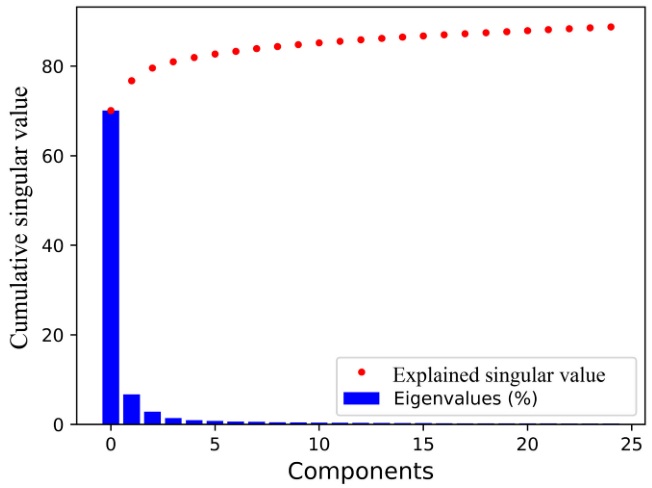

Fig. 6. Variance explained by each component in PCA.

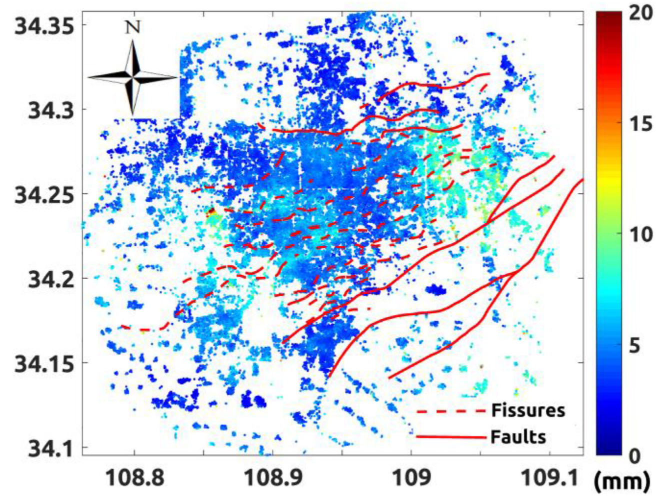

Fig. 5. SD of deformation time series of different SAR sensors in overlapping time periods.

Unlike linear interpolation [67], when using the overlapped deformation to fuse and link different sensors or track deformation time series, the atmospheric error, orbit error, and DEM error phase should be corrected. Only Gaussian noise is permitted in deformation time series. Therefore, RSLS is recommended.

In order to analyze the accuracy of the deformation time series, we estimate the standard deviation (SD) of the deformation time series from different sensors in overlapping time periods, as shown in Fig. 5. Specifically, we used 9 ALOS/PALSAR-2 images and overlapping data in TerraSAR-X images and Sentinel-1A SAR images to estimate the SD. Different SAR sensor wavebands have different sensitivity to deformation, so their measurement accuracy differs. The SD between them is within 20 mm. Cross-validation results of deformation time series obtained by different sensors prove that our estimated deformation time series are reliable.

B. Spatiotemporal Deformation Pattern Analysis

Previous research has mapped ground deformation characteristics using different sensors and across different time spans [40], [44]–[47]. With our newly developed continuously updating multisensor InSAR deformation time-series approach, we were able to map the evolution of long-term surface deformation in Xi'an from January 3, 2007 to February 12, 2021, which is well suited to large-scale, near-real-time monitoring.

In order to map evolution characteristics and spatiotemporal scope, we used the tICA algorithm [61], [62] to investigate the spatiotemporal evolution of Xi'an surface deformation from January 3, 2007 to February 12, 2021. The tICA assumes that the source signal is temporally independent in order to fit the spatiotemporal deformation characteristics. We assumed that there are four independent patterns of temporal evolution deformation. Principal component analysis (PCA) was used to explore the reliability of our hypothesis of four ICs, as shown in Fig. 6. The eigenvalues of the first four components can explain approximately 80% (70.1%, 6.7%, 2.8%, 1.4%) of the cumulative signal variance.

Then, the FastICA algorithm [61], [62] was employed to decompose the mixed-signal matrix stacking deformation time series $\mathbf{U}$ with dimensions of 66 380 $\times$ 192 (wherein 66 380 represents the number of selected coherent pixels and 192 represents the number of SAR images) into a set of four statistically independent sources in temporal $\mathbf{S} = [s_1, s_2, s_3, s_4]^T$ $(s_i = [s_i^0, s_i^1, \ldots, s_i^{191}])$ (see Fig. 7) and mixing $\mathbf{A} = [a_1, a_2, a_3, a_1]$ $(a_i = [a_i^1, a_i^2, \ldots, a_i^{66\,380}]^T)$ matrices (see Fig. 8). In the FastICA algorithm, fixed-point iteration is used to derive the converged solution of mixing matrix $\mathbf{A}$ and source matrix $\mathbf{S}$ by maximizing the temporal non-Gaussianity of sources [59].

The temporal source matrices S_1(IC1), S_2(IC2), S_3(IC3), and S_4(IC4) in Fig. 7 show four independent patterns of deformation evolution over time. The mixing matrices a_1, a_2, a_3, and a_4 capture the relative contribution of the independent temporal

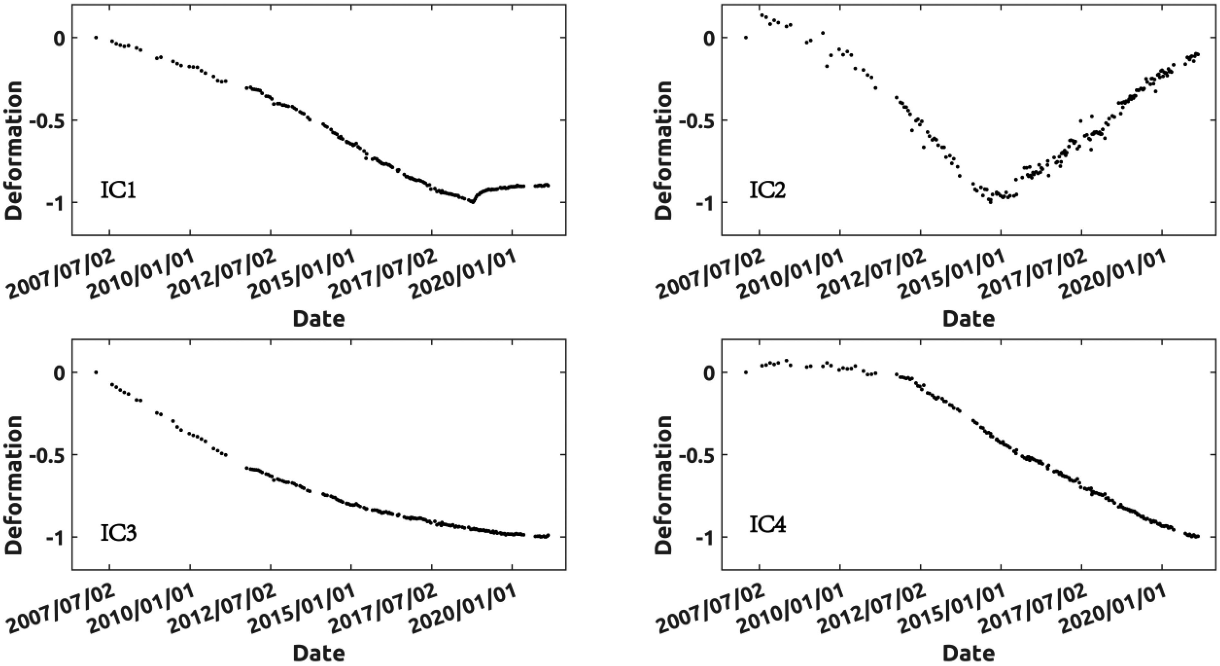

Fig. 7. Four different temporal deformation patterns, IC1 to IC4, obtained by ICA.

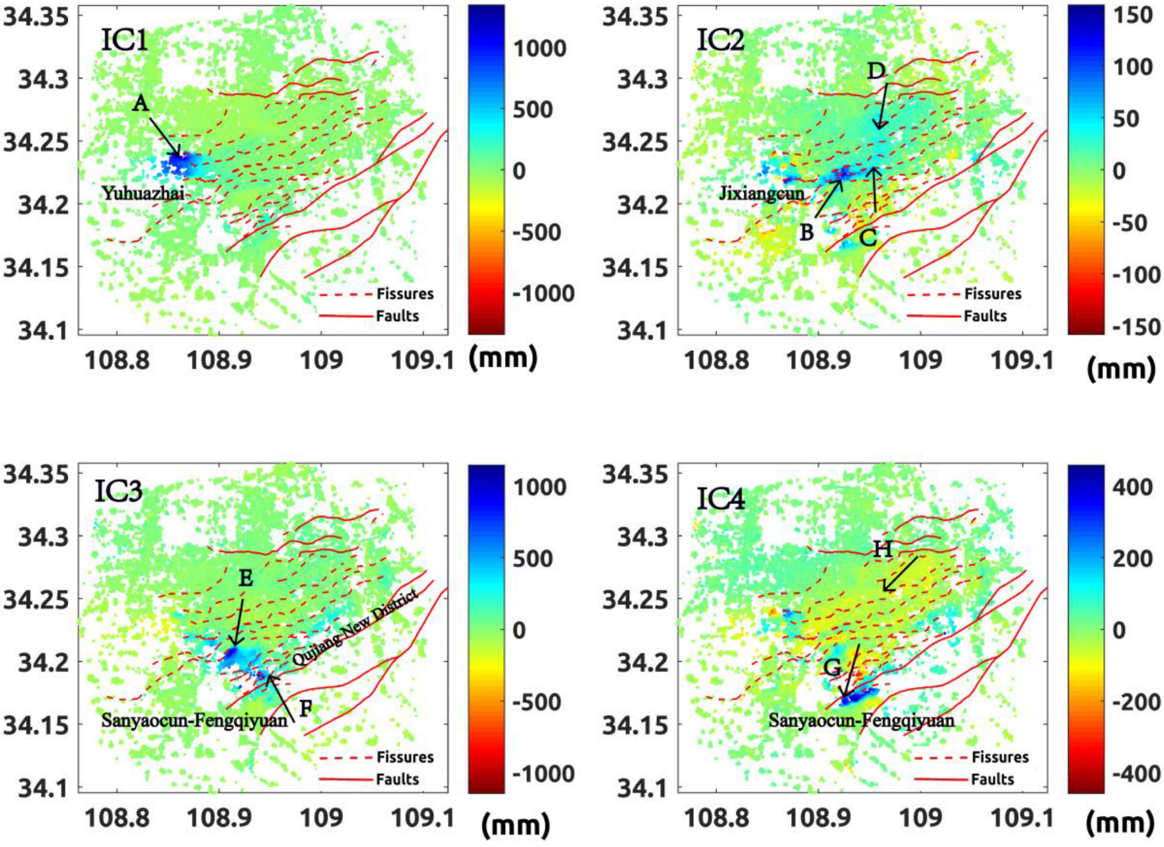

Fig. 8. Four different spatial deformation patterns, IC1 to IC4, obtained by ICA. Points indicated by arrows A–H are shown in Fig. 9.

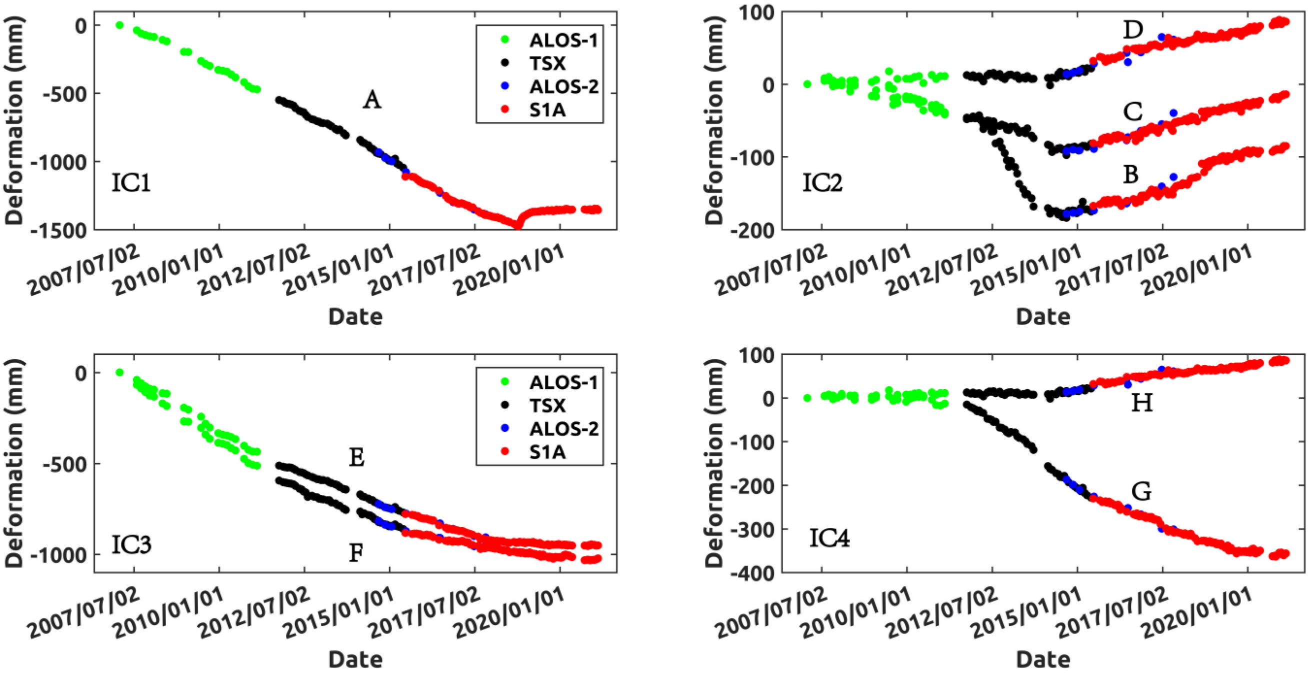

Fig. 9. Time-series deformation A–H. The eight points were selected according to their spatial deformation patterns to show the evolution of temporal deformation from January 3, 2007 to February 12, 2021.

components a_1(IC1), a_2(IC2), a_3(IC3), and a_4 (IC4), respectively (see Fig. 8). Thus, there are four spatial deformation areas with different time evolution characteristics.

IC1 mapped the rebound deformation characteristics upon ceasing groundwater exploitation and the effect of the subsequent artificial water injection, as seen in the uplift at point A in Fig. 9. This is distinct from a rebound area in Xi'an introduced in [40]. Instead, IC1 mapped the spatial range of rebound deformation in Yuhuazhai, well south and west of Xi'an.

In terms of temporal evolution, IC2 maps a deformation pattern of land subsidence and uplift around Jixiangcun. However, it is irregular in space and controlled by ground fissures. The three points B, C, and D were selected in IC2 to show the deformation time series in Fig. 9.

IC3 mapped regions in Sanyaocun-Fengqiyuan and Qujiang New District that are experiencing subsidence, where the deformation rate gradually slows over the study period. The two points E and F were selected in IC3 to show the deformation time series in Fig. 9.

The temporal deformation pattern in IC4 shows that no deformation was found from 2007 to 2011, at which point a linear deformation feature began and continues to the present. The two points G and H were selected in IC4 to show the deformation time series in Fig. 9.

In IC2, points B, C, and D show the same deformation time-series pattern at the same magnitude (see Fig. 9). However, in IC3 and IC4, we can see the influence of the CAF in the patterns of deformation time-series evolution. Areas to the north (see Fig. 9, point E) and south (see Fig. 9, point G) of the fault show different temporal deformation patterns. In IC3, it is difficult to separate the two similar time deformation characteristics at points E and F.

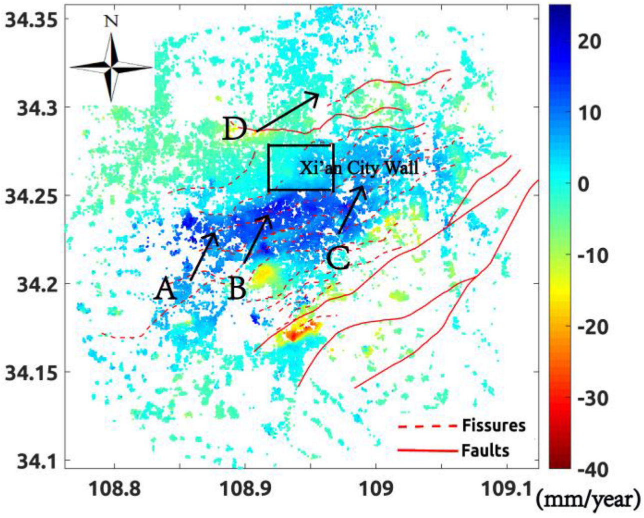

Fig. 10. Deformation rate from 2019 to 2021. Points A–D are shown in Fig. 11.

C. Future Deformation Trends

Large-scale exploitation of confined water in Xi'an since the 1970s can be divided into three stages: exploitation, overexploitation, and cessation [43]. The main areas of land subsidence have experienced three stages: initial subsidence, serious subsidence, and then gradual stability [68]. Before 1970, the confined water level depth was 10–20 m. The land subsidence

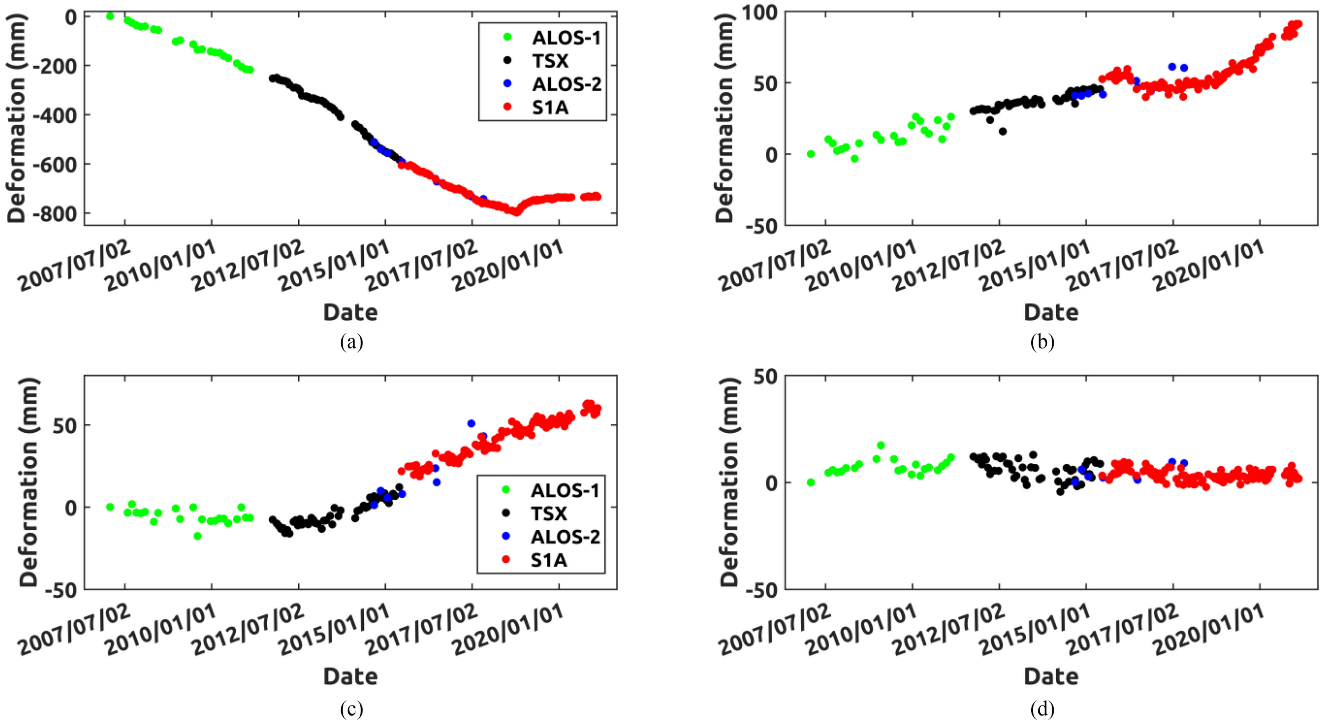

(a) (b)

(c) (d)

Fig. 11. Time-series deformation (A)–(D). The four points are selected to show the evolution of uplift deformation.

area located in the east of Xi'an had a slow average subsidence rate of 2 mm per year. Between 1970 and 1995, due to economic development and urbanization, groundwater overexploitation increased rapidly to over 1000 pumping wells, leading to an increase in confined water level depth of approximately 100 m. As surface subsidence rates increased, the subsidence area expanded rapidly to the south of Xi'an, concentrated in the area of the Second Ring Road. During this period, regional subsidence centers and seven ground fissures were discovered.

From 1996 to 2002, groundwater exploitation was restricted in order to alleviate land subsidence, and the confined water level depth began to slowly move closer to the surface. Land subsidence within the Second Ring Road gradually slowed, and the subsidence center moved to the south. A total of 13 ground fissures were found. Overexploitation of groundwater leads to decreases in groundwater levels. Although the confined aquifer is elastic, continuous overexploitation of groundwater can lead to irrevocable confined aquifer deformation, which further leads to land subsidence [69].

Beginning in 2002, the primary water source for the region transitioned from subsurface withdrawal to water from the Heihe River and its associated dam projects. A cumulative water volume of 1 552 800 m^3 was recharged to the subsurface between 2002 and 2017. By 2015, the water level rose to a depth of 90–100 m and land subsidence began to slow. When groundwater exploitation stops and the confined aquifer water level recovers, land subsidence does not stop immediately; rather, after a period of continuous subsidence, it stops or rebounds. The deformation pattern can be divided into immediate elastic recovery deformation and time-dependent viscoelastic recovery deformation [69].

We mapped the rate of deformation over the last two years (see Fig. 10; the rectangular range represents the city wall of Xi'an). It is clear that the extent of the area of uplift deformation is great. The uplift deformation boundary in the south is controlled by ground fissures.

According to the spatial deformation characteristics shown in Fig. 10, we selected four feature points to show the evolution of deformation from January 3, 2007 to February 12, 2021 (see Fig. 11). The time series of point A shows a pattern of decline followed by a rebound, with a decreasing magnitude of rebound deformation. The deformation time series of point B shows slow surface deformation prior to 2007. At point C, uplift deformation started in approximately 2012. Point D exemplifies the stable areas.

The contours of confined water in 1960, 1968, 1977, 1983, 1995, and 2004 are mapped in Fig. 12. The rectangular range represents the city wall of Xi'an. From 1960 to 2004, a funnel of declining groundwater levels is seen. In 1960, the confined water in the Xi'an area flowed from south to north. The hydraulic gradient was 2–3%, and the confined water level depth was 10–20 m. In 1968, exploitation of groundwater began and the groundwater flow began to shift, but no funnel of groundwater level decline was found. In 1977, a large amount of confined water was exploited. Three confined water level funnels appeared, and the confined water level dropped to 30–40 m. In 1983, the confined water level funnels continued to expand. In 1995, the funnel of groundwater level decline reached its maximum and the lowest depth of confined water level exceeded 100 m.

In 2004, the groundwater level began to rise. Since groundwater exploitation has ceased, we can expect the gradual recovery

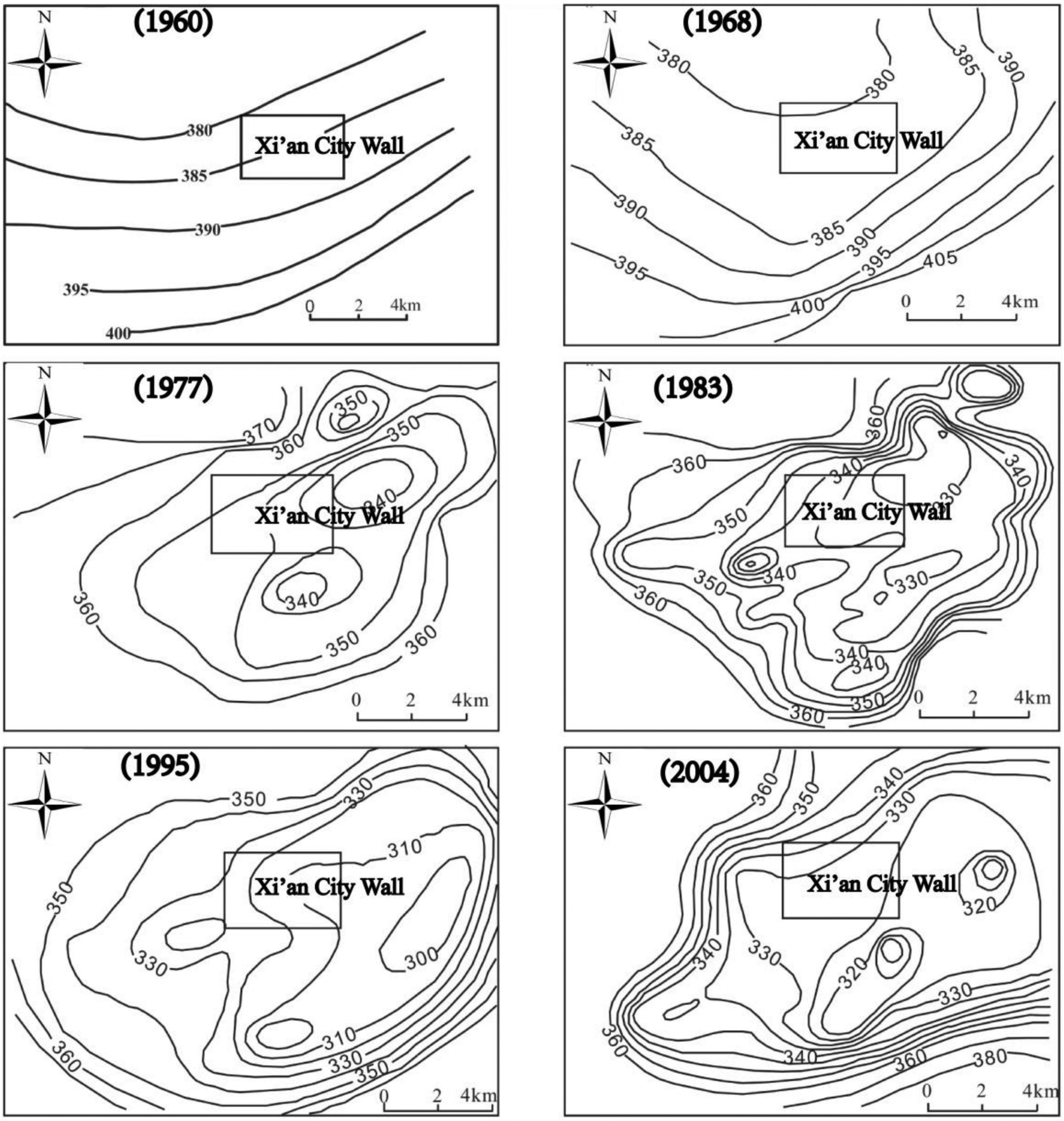

Fig. 12. Contour map of confined water from 1960 to 2004 [70].

of the confined groundwater level in Xi'an, accompanied by elastic recovery deformation and time-dependent viscoelastic recovery deformation [69]. The uplift deformation areas in Fig. 10 are consistent with the funnel of groundwater level [70]. As the confined water level continues to move closer to the surface, uplift deformation is inevitable. Uplift deformation is a process of interaction among ground fissures, faults, and groundwater.

Since 1996, Yuhuazhai has experienced the most severe deformation seen in the study area. From 1996 to 2016, the accumulated land subsidence in this area reached 1.8–2 m [71]. However, the land subsidence stopped suddenly in mid-October 2018 and rebounded over 130 mm. This was because of artificial water injection in combination with halting exploitation of groundwater at more than 45 deep wells. Due to the larger

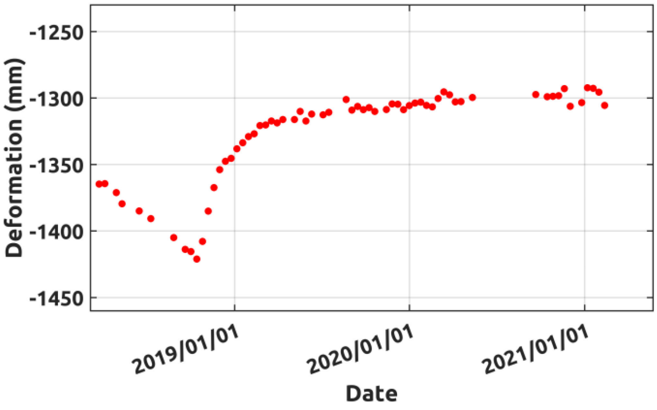

Fig. 13. Rebound deformation time series.

difference in phreatic aquifer head on both sides of the ground fissure at Yuhuazhai, the water injection allowed groundwater to the south of the fissure to recover rapidly. This can be interpreted as immediate elastic recovery deformation [40], [69]. Fig. 13 shows that the deformation has tended to be stable since then.

V. CONCLUSION

Both the initial occurrence and evolution of land subsidence in the Xi'an area of China are closely related to groundwater levels. We introduced a long-term continuously updating multisensor InSAR deformation time-series algorithm to study land subsidence in Xi'an from 2007 to 2021. We found that the Yuhuazhai area has tended to be stable since late 2018, ending severe deformation processes of the preceding two and a half decades. We also found a decline in the deformation rate of other areas experiencing land subsidence. We identified a large area of uplift deformation in response to water level recovery. In the future, we can expect to see uplift deformation across a large area in Xi'an. Our proposed approach is an effective tool to continuously update long-term studies in near-real-time using one- or multidimensional deformation time series, leveraging the massive quantities of multisensor and multitrack SAR data. This approach can significantly improve the temporal resolution of deformation and potentially provide early warning of geohazard disasters.

ACKNOWLEDGMENT

ALOS/PALSAR-1/2 data were provided by JAXA, Japan, TerraSAR-X data by DLR, and Sentinel-1A are copyrighted to the European Space Agency.

REFERENCES

[1] A. K. Gabriel, R. M. Goldstein, and H. A. Zebker, "Mapping small elevation changes over large areas-differential radar interferometry," *J. Geophys. Res. Solid Earth*, vol. 94, no. B7, pp. 9183–9191, 1989.

[2] G. Peltzer, "Evidence of nonlinear elasticity of the crust from the Mw7.6 Manyi (Tibet) earthquake," *Science*, vol. 286, no. 5438, pp. 272–276, 1999.

[3] Z. Lu and D. Dzurisin, *InSAR Imaging of Aleutian Volcanoes: Monitoring a Volcanic Arc From Space* (Geophysical Sciences). Berlin, Germany: Springer, 2014.

[4] C. Zhao, Z. Lu, Q. Zhang, and J. D. L. Fuente, "Large-area landslide detection and monitoring with ALOS/PALSAR imagery data over northern California and southern Oregon, USA," *Remote Sens. Environ.*, vol. 124, pp. 348–359, 2012.

[5] D. A. Schmidt and R. Burgmann, "Time-dependent land uplift and subsidence in the Santa Clara Valley, California, from a large interferometric synthetic aperture radar data set," *J. Geophys. Res. Solid Earth*, vol. 108, no. B9, 2416, 2003.

[6] F. Amelung, D. L. Galloway, J. W. Bell, H. A. Zebker, and R. J. Laczniak "Sensing the ups and downs of lasvegas: InSAR reveals structural control of land subsidence and aquifer-system deformation," *Geology*, vol. 27, no. 6, 1999, Art. no. 483.

[7] F. Qu *et al.*, "Mapping ground deformation over Houston–Galveston, Texas using multi-temporal InSAR," *Remote Sens. Environ.*, vol. 169, pp. 290–306, 2015.

[8] F. Cigna and D. Tapete. "Present-day land subsidence rates, surface faulting hazard and risk in Mexico city with 2014–2020 Sentinel-1 IW InSAR," *Remote Sens. Environ.*, vol. 253, 2021, Art. no. 112161.

[9] M. Motagh, Y. Djamour, T. R. Walter, H. U. Wetzel, and S. Arabi. "Land subsidence in Mashhad Valley, northeast Iran: Results from InSAR, levelling and GPS," *Geophys. J. Int.*, vol. 168, no. 2, pp. 518–526, 2007.

[10] K. Modis and D. Sideri "Spatiotemporal estimation of land subsidence and ground water level decline in West Thessaly Basin, Greece," *Natural Hazards*, vol. 76, pp. 939–954, 2015. [Online]. Available: https://doi.org/10.1007/s11069-014-1528-2

[11] L. Solari, A. Ciampalini, F. Raspini, S. Bianchini, and S. Moretti, "PSInSAR analysis in the Pisa urban area (Italy): A case study of subsidence related to stratigraphical factors and urbanization," *Remote Sens.*, vol. 8, no. 2, 2016, Art. no. 120. [Online]. Available: https://doi.org/10.3390/rs8020120

[12] B. Chen *et al.*, "Investigating land subsidence and its causes along Beijing high-speed railway using multi-platform InSAR and a maximum entropy model," *Int. J. Appl. Earth Obs. Geoinf.*, vol. 96, 2021, Art. no. 102284.

[13] A. Ferretti, C. Prati, and F. Rocca, "Permanent scatterers in SAR interferometry," *IEEE Trans. Geosci. Remote Sens.*, vol. 39, no. 1, pp. 8–20, Jan. 2001.

[14] P. Berardino, G. Fornaro, R. Lanari, and E. Sansoti, "A new algorithm for surface deformation monitoring based on small baseline differential SAR interferograms," *IEEE Trans. Geosci. Remote Sens.*, vol. 40, no. 11, pp. 2375–2383, Nov. 2002.

[15] C. Werner, U. Wegmuller, T. Strozzi, and A. Wiesmann, "Interferometric point target analysis for deformation mapping," in *Proc. Int. Geosci. Remote Sens. Symp.*, Toulouse, France, Jul. 21–25, 2003, vol. 7, pp. 4362–4364.

[16] A. Hooper, H. Zebker, P. Segall, and B. Kampes, "A new method for measuring deformation on volcanoes and other natural terrains using InSAR persistent scatterers," *Geophys. Res. Lett.*, vol. 31, L23611, 2004, doi: 10.1029/2004gl021737.

[17] B. Kampes, *Radar Interferometry: Persistent Scatterer Technique*. Dordrecht, The Netherlands: Springer, 2006.

[18] A. Hooper, "A multi-temporal InSAR method incorporating both persistent scatterer and small baseline approaches," *Geophys. Res. Lett.*, vol. 35, pp. 96–106, 2008, doi: 10.1029/2008gl034654.

[19] A. Ferretti, A. Fumagalli, F. Novali, C. Prati, F. Rocca, and A. Rucci, "A new algorithm for processing interferometric data-stacks: SqueeSAR," *IEEE Trans. Geosci. Remote Sens.*, vol. 49, no. 9, pp. 3460–3470, Sep. 2011.

[20] A. Parizzi and R. Brcic, "Adaptive InSAR stack multilooking exploiting amplitude statistics: A comparison between different techniques and practical results," *IEEE Geosci. Remote Sens. Lett.*, vol. 8, no. 3, pp. 441–445, May 2011.

[21] S. Wu, L. Zhang, X. Ding, and D. Perissin, "Pixel-wise MTInSAR estimator for integration of coherent point selection and unwrapped phase vector recovery," *IEEE Trans. Geosci. Remote Sens.*, vol. 57, no. 5, pp. 2659–2668, May 2019.

[22] F. Hu, J. Wu, L. Chang, and R. F. Hanssen, "Incorporating temporary coherent scatterers in multi-temporal InSAR using adaptive temporal subsets," *IEEE Trans. Geosci. Remote Sens.*, vol. 57, no. 10, pp. 7658–7670, Oct. 2019.

[23] B. Wang, C. Zhao, Q. Zhang, and Y. Liu, " An improved SAR interferogram denoising method based on principal component analysis and the Goldstein filter," *Remote Sens. Lett.*, vol. 9, no. 1, pp. 81–90, 2018, doi: 10.1080/2150704X.2017.1392633.

[24] M. Crosetto, O. Monserrat, M. Cuevas-González, N. Devanthéry, and B. Crippa, "Persistent scatterer interferometry: A review," *ISPRS J. Photogramm. Remote Sens.*, vol. 115, pp. 78–89, 2015.

[25] B. Osmanoğlu *et al.*, "Time series analysis of InSAR data: Methods and trends," *ISPRS J. Photogramm. Remote Sens.*, vol. 115, pp. 90–102, 2016.

[26] D. H. T. Minh, R. Hanssen, and F. Rocca, "Radar interferometry: 20 years of development in time series techniques and future perspectives," *Remote Sens.*, vol. 12, no. 9, 2020, Art. no. 1364. [Online]. Available: https://doi.org/10.3390/rs12091364

[27] J.-W. Kim, Z. Lu, Y. Jia, and C. K. Shum, "Ground subsidence in Tucson, Arizona, monitored by time-series analysis using multi-sensor InSAR datasets from 1993 to 2011," *ISPRS J. Photogramm. Remote Sens.*, vol. 107, pp. 126–141, 2015.

[28] D. McAlpin and F. J. Meyer, "Multi-sensor data fusion for remote sensing of post-eruptive deformation and depositional features at redoubt volcano," *J. Volcanol. Geothermal. Res.*, vol. 259, pp. 414–423, 2013.

[29] G. Herrera *et al.*, "Multi-sensor advanced DInSAR monitoring of very slow landslides: The Tena valley case study (Central spanish pyrenees)," *Remote Sens. Environ.*, vol. 128, pp. 31–43, 2013.

[30] J. Hu *et al.*, "Resolving three-dimensional surface displacements from InSAR measurements: A review," *Earth-Sci. Rev.*, vol. 133, no. 1, pp. 1–17, 2014.

[31] A. Pepe and F. Calò, "A review of interferometric synthetic aperture RADAR (InSAR) multi-track approaches for the retrieval of earth's surface

displacements," *Appl. Sci.*, vol. 7, no. 12, 2017, Art. no. 1264. [Online]. Available: https://doi.org/10.3390/app7121264

[32] I. Zinno, F. Casu, C. D. Luca, S. Elefante, R. Lanari, and M. Manunta, "A cloud computing solution for the efficient implementation of the p-sbas dinsar approach," *IEEE J. Sel. Topics Appl. Earth Meas. Remote Sens.*, vol. 10, no. 3, pp. 802–817, Mar. 2017.

[33] J. Hu, X. L. Ding., Z. W. Li, J. J. Zhu, Q. Sun, and L. Zhang, "Kalman-filter-based approach for multisensor, multitrack, and multitemporal InSAR," *IEEE Trans. Geosci. Remote Sens.*, vol. 51, no. 7, pp. 4226–4239, Jul. 2013.

[34] M. Dalaison and R. Jolivet, "A Kalman filter time series analysis method for InSAR," *J. Geophys. Res., Solid Earth*, vol. 125, no. 7, 2020, Art. no. e2019JB019150. [Online]. Available: https://doi.org/10.1029/2019JB019150

[35] H. Ansari, F. De Zan, and R. Bamler, "Sequential estimator: Toward efficient InSAR time series analysis," *IEEE Trans. Geosci. Remote Sens.*, vol. 55, no. 10, pp. 5637–5652, Oct. 2017.

[36] B. Xu, Z. Li, Y. Zhu, J. Shi, and G. Feng, "Kinematic coregistration of sentinel-1 TOPSAR images based on sequential least squares adjustment," *IEEE J. Sel. Topics Appl. Earth Observ. Remote Sens.*, vol. 13, pp. 3083–3093, Jun. 2020.

[37] Z. Ma, M. Jiang, and T. Huang, "A sequential approach for sentinel-1 TOPS time-series co-registration over low coherence scenarios," *IEEE Trans. Geosci. Remote Sens.*, vol. 69, no. 6, pp. 4818–4826, Jun. 2021.

[38] B. Wang, C. Zhao, Q. Zhang, Z. Lu, Z. Li, and Y. Liu, "Sequential estimation of dynamic deformation parameters for SBAS-InSAR," *IEEE Geosci. Remote Sens. Lett.*, vol. 17, no. 6, pp. 1017–1021, Jun. 2020.

[39] B. Wang *et al.*, "Update two-dimensional SAR offset tracking deformation time series with complex sequential least squares estimation," *Remote Sens. Lett.*, vol. 12, no. 3, pp. 247–256, 2021, doi: 10.1080/2150704X.2020.1864055.

[40] B. Wang, C. Zhao, Q. Zhang, and M. Peng, "Sequential InSAR time series deformation monitoring of land subsidence and rebound in Xi'an, China," *Remote Sens.*, vol. 11, no. 23, 2019, Art. no. 2854. [Online]. Available: https://doi.org/10.3390/rs11232854

[41] J. B. Peng, *Geohazards of Xi'an Ground Fissures*. Beijing, China: Science Press, 2012, pp. 267–316, (in Chinese).

[42] J. Peng, W. Qu, J. Ren, Q. Zhang, and F. Wang, "Geological factors for the formation of Xi'an ground fractures," *J. Earth Sci.*, vol. 29, no. 2, pp. 468–478, 2018.

[43] Y. Q. Wang, Z. F. Wang, and W. C. Cheng, "A review on land subsidence caused by groundwater withdrawal in Xi'an, China," *Bull. Eng. Geol. Environ.*, vol. 78, pp. 2851–2863, 2019. [Online]. Available: https://doi.org/10.1007/s10064-018-1278-6

[44] C. Y. Zhao, Q. Zhang, X. L. Ding, Z. Lu, C. S. Yang, and X. M. Qi, "Monitoring of land subsidence and ground fissures in Xian, China 2005–2006: Mapped by SAR interferometry," *Environ. Geol. (Berlin)*, vol. 58, no. 7, pp. 1533–1540, 2009.

[45] F. Qu, Q. Zhang, Z. Lu, C. Zhao, C. Yang, and J. Zhang, "Land subsidence and ground fissures in Xi'an, China 2005–2012 revealed by multi-band InSAR time-series analysis," *Remote Sens. Environ.*, vol. 155, pp. 366–376, 2014.

[46] M. Li, D. Ge, B. Liu, L. Zhang, Y. Wang, and X. Guo, "Research on development characteristics and failure mechanism of land subsidence and ground fissure in Xi'an, monitored by using time-series SAR interferometry," *Geomatics, Natural Hazards Risk*, vol. 10, no. 1, pp. 699–718, 2019, doi: 10.1080/19475705.2018.1542350.

[47] M. Peng, C. Zhao, Q. Zhang, Z. Lu, and Z. Li, "Research on spatiotemporal land deformation (2012–2018) over Xi'an, China, with multi-sensor SAR datasets," *Remote Sens.*, vol. 11, no. 6, 2019, Art. no. 664. [Online]. Available: https://doi.org/10.3390/rs11060664

[48] H. Yu, Y. Lan, J. Xu, D. An, and H. Lee, "Large-scale L^0-norm and L^1 -norm 2-D phase unwrapping," *IEEE Trans. Geosci. Remote Sens.*, vol. 55, no. 8, pp. 4712–4728, Aug. 2017.

[49] H. Yu, H. Lee, T. Yuan, and N. Cao, "A novel method for deformation estimation based on multibaseline InSAR phase unwrapping," *IEEE Trans. Geosci. Remote Sens.*, vol. 56, no. 9, pp. 5231–5243, Sep. 2018.

[50] H. Yu, Y. Lan, Z. Yuan, J. Xu, and H. Lee, "Phase unwrapping in InSAR : A review," *IEEE Geosci. Remote Sens. Mag.*, vol. 7, no. 1, pp. 40–58, Mar. 2019.

[51] T. R. Lauknes, H. A. Zebker, and Y. Larsen, "InSAR deformation time series using an L1-norm small-baseline approach," *IEEE Trans. Geosci. Remote Sens.*, vol. 49, no. 1, pp. 536–546, Jan. 2011.

[52] Y. X. Yang, "Robust Bayesian estimation," *J. Geodesy*, vol. 65, no. 3, pp. 145–150, 1991.

[53] W. B. Huang, *Modern Adjustment Theory and Its Application*. Beijing, China: PLA Press, 1992.

[54] Q. Zhao *et al.*, "Generation of long-term InSAR ground displacement time-series through a novel multi-sensor data merging technique: The case study of the Shanghai coastal area," *ISPRS J. Photogramm. Remote Sens.*, vol. 154, pp. 10–27, 2019.

[55] M. Shirzaei, "A seamless multitrack multitemporal InSAR algorithm," *Geochem., Geophys., Geosyst.*, vol. 16, no. 5, pp. 1656–1669, 2015.

[56] P. Comon, "Independent component analysis, a new concept?," *Signal Process.*, vol. 36, no. 3, pp. 287–314, 1994.

[57] S. K. Ebmeier, "Application of independent component analysis to multitemporal InSAR data with volcanic case studies," *J. Geophys. Res., Solid Earth*, vol. 121, no. 12, pp. 8970–8986, 2016.

[58] E. Chaussard and T. G. Farr, "A new method for isolating elastic from inelastic deformation in aquifer systems: Application to the San Joaquin Valley, CA," *Geophys. Res. Lett.*, vol. 16, pp. 10800–10809, 2019.

[59] H. Liang, L. Zhang, Z. Lu, and X. Li, "Nonparametric estimation of DEM error in multitemporal InSAR," *IEEE Trans. Geosci. Remote Sens.*, vol. 57, no. 12, pp. 10004–10014, Dec. 2019.

[60] M. E. Gaddes, A. Hooper, M. Bagnardi, H. Inman, and F. Albino, "Blind signal separation methods for InSAR: The potential to automatically detect and monitor signals of volcanic deformation," *J. Geophys. Res., Solid Earth*, vol. 123, no. 11, pp. 10–226, 2018.

[61] A. Hyvarinen, "Fast and robust fixed-point algorithms for independent component analysis," *IEEE Trans. Neural Netw.*, vol. 10, no. 3, pp. 626–634, May 1999.

[62] A. Hyvärinen and E. Oja, "Independent component analysis: Algorithms and applications," *Neural Netw.*, vol. 13, pp. 411–430, 2000.

[63] Y.-N. N. Lin, M. Simons, E. A. Hetland, P. Muse, and C. DiCaprio, "A multiscale approach to estimating topographically correlated propagation delays in radar interferograms," *Geochem., Geophys., Geosyst*, vol. 11, no. 9, 2010, Art. no. Q09002.

[64] H. Liang, L. Zhang, X. Ding, Z. Lu, and X. Li, "Toward mitigating stratified tropospheric delays in multitemporal InSAR: A quadtree aided joint model," *IEEE Trans. Geosci. Remote Sens.*, vol. 57, no. 1, pp. 291–303, Jan. 2019.

[65] Y. Chen *et al.*, "Generic atmospheric correction model for interferometric synthetic aperture radar observations," *J. Geophys. Res., Solid Earth*, vol. 123, pp. 9202–9222, 2018.

[66] Y. Du, L. Zhang, G. Feng, Z. Lu, and Q. Sun, "On the accuracy of topographic residuals retrieved by MTInSAR," *IEEE Trans. Geosci. Remote Sens.*, vol. 55, no. 2, pp. 1053–1065, Feb. 2017.

[67] S. Usai, "A least squares database approach for SAR interferometric data," *IEEE Trans. Geosci. Remote Sens.*, vol. 41, no. 4, pp. 753–760, Apr. 2003.

[68] J. J. Zhang, H. X. Zhan, M. S. Zhang, H. Tao, Y. Dong, and C. M. Xu, "Study on the seepage deformation induce ground fissures caused and land subsidence in Xi'an," *J. Eng. Geol.*, vol. 26, pp. 301–309, 2018.

[69] Y. Zhang, J. Wu, Y. Xue, Z. Wang, Y. Yao, and X. Yan, "Land subsidence and uplift due to long-term groundwater extraction and artificial recharge in Shanghai, China," *Hydrol. J.*, vol. 23, pp. 1851–1866, 2015.

[70] Y. Dong, M. S. Zhang, J. Liu, X. L. Zhang, and L. Feng, "Coupling relationship between groundwater and ground fissures of land subsidence in Xi'an city and risk prevention and control technology," *J. Geol. Hazards Environ. Preservation*, vol. 2, pp. 95–102, 2019.

[71] Z. J. Jun, Z. H. Xin, Z. M. Sheng, L. I. Yong, D. Yin, and Z. Q. Gui, "Preliminary study of land subsidence in the f4 ground fissure, Yuhuazhai area, Xi'an, China," *J. Geol. Hazards Environ. Preservation*, vol. 4, pp. 31–37, 2017.

Baohang Wang (Student Member, IEEE) was born in Xianyang, China, in 1992. He received the B.S. degree in surveying engineering from Longyan University, Longyan, China, in 2015, and the M.Sc. degree in geodesy and surveying engineering from Chang'an University, Xi'an, China, in 2018, where he is currently working toward the Ph.D. degree.

His research interests include algorithm developments for multitemporal synthetic aperture radar interferometry and the applications on dynamic ground deformation monitoring.

Chaoying Zhao (Senior Member, IEEE) received the M.S. and Ph.D. degrees in geodesy and surveying engineering from Chang'an University, Xi'an, China, in 2002 and 2009, respectively.

He is currently a Professor of geodesy and survey engineering with Chang'an University. His research interests include the development of different InSAR methods, including dynamic SAR/InSAR data processing with the sequential least-squares norm, large gradient surface deformation with SAR offset tracking method, and their applications in geohazard identification, monitoring, and mechanism explanations, including land subsidence, ground fissures, landslide, and mining-induced collapse.

Qin Zhang (Member, IEEE) received the Ph.D. degree in geodesy from Wuhan University, Wuhan, China, in 2002.

She is currently a Professor of geodesy and survey engineering with Chang'an University, Xi'an, China. She is currently working on the high-precision geodetic data processing and algorithm development including GNSS, and InSAR, and the monitoring and early forecast on geohazards, including land subsidence, ground fissures, and landslide.

Zhong Lu (Senior Member, IEEE) received the B.S. and M.S. degrees in geophysics from Peking University, Beijing, China, in 1989 and 1992, respectively, and the Ph.D. degree in geophysics from the University of Alaska, Fairbanks, AK, USA, in 1996.

He is currently a Professor and the Endowed Shuler-Foscue Chair with the Huffington Department of Earth Sciences, Southern Methodist University, Dallas, TX, USA. He is also a Principal Investigator of projects funded by NASA, ESA, JAXA, DLR, and USGS on the study of land surface deformation using satellite interferometric synthetic aperture radar (InSAR) imagery. He has authored more than 45 and coauthored 90 peer-reviewed journal articles and book chapters focused on InSAR techniques and applications. His research interests include technique developments of SAR, InSAR, and their applications on natural hazard monitoring and natural resource characterization.

Antonio Pepe (Senior Member, IEEE) received the Laurea degree in electronic engineering and the Ph.D. degree in electronic and telecommunication engineering from the University of Naples Federico II, Naples, Italy, in 2000 and 2007, respectively.

He joined the Istituto per il Rilevamento Elettromagnetico dell'Ambiente, Italian National Research Council (CNR), Naples, where he currently holds a permanent position of Senior Researcher.More recently, he has developed research activities for the generation of DInSAR products through multiplatform/multiangle and the new generation SAR instruments, the generation of hybrid scan SAR-to-stripmap DInSAR analyses, the integration of SAR and optical images, and the analysis of land changes in flooded areas. His main research interests include the development of advanced differential synthetic aperture radar interferometry (DInSAR) algorithms for the monitoring of surface deformation phenomena induced by subsidence, volcano activities, and earthquakes, with a particular interest toward the phase unwrapping problems.